

Role of sills in the development of volcanic fields: Insights from lidar mapping surveys of the San Rafael Swell, Utah

1 Abstract

Analysis of airborne and terrestrial lidar data demonstrates that $>0.4 \text{ km}^3$ of magma cooled in sills at shallow ($<1 \text{ km}$) depth in the now eroded Pliocene San Rafael Swell distributed volcanic field, Utah (USA). The volumes of each of seven sills are estimated from 3D models of the lidar data and range from $10^{-4}\text{--}10^{-1} \text{ km}^3$. Directions of magma flow during emplacement are interpreted from precise sill thickness measurements and measurements of linear vertical offsets within the sills, helping to identify feeder conduits and dikes; 3D map relationships derived from lidar data demonstrate that magma flowed into and out of sills from these active dikes and eruptive conduits. Mapped sill volumes account for $>92\%$ of intrusive material within the 50 km^2 study area. We conclude that sills played a significant role in modifying eruption dynamics during activity in San Rafael, and suggest that monitoring of sill inflation and deflation in active distributed volcanic fields may provide key information about unrest and potential eruption dynamics.

2 Introduction

Intermediate to shallow crustal storage of pre- and syn-eruption magma modulates magma supply rate in many volcanic systems. At Mount St. Helens (A.D. 1980 eruption; USA) and Parcuitin (A.D. 1943 eruption; Mexico), magma supply rate is thought to have been influenced by the presence of shallow ($<10 \text{ km}$), temporary magma storage [Cashman and McConnell, 2005] and by the length of storage time [Scandone et al., 2007]. Erlund et al. [2010] identified increasing amounts of shallow crust ($\leq 4 \text{ km}$ depth) assimilated at Parcuitin over the 9-year eruption, and concluded that a shallow intrusion network formed early and caused later eruptive products to be more effusive. On shorter timescales, gas may segregate preferentially into conduits above shallow sills, increasing volumetric flow in the conduit and intensifying the eruption [Conte, 2000, Pioli et al., 2009]. Sill-like intrusions into shallow magma chambers have recently been geodetically linked with interferometric synthetic aperture radar (InSAR) and seismic monitoring to eruptions at Tungurahua, Ecuador [Biggs et al., 2010] and Eyjafjallajökull, Iceland [Tarasewicz et al., 2012]. These models and observations suggest that it is critical to understand the volume, depth and distribution of sills in volcanic fields in order to forecast eruption dynamics and the evolution of volcanic systems.

In young volcanic fields, such as the one around Parcutin [Connor, 1990], it is not possible to directly observe the shallow plumbing system. Here, we use lidar technology to map part of the eroded San Rafael Swell (UT) volcanic field. These data demonstrate that sills are prevalent at shallow depths (<1 km), modulated magma flow in eruptive conduits, and likely influenced eruption dynamics within this volcanic field.

3 Geologic Description

The San Rafael volcanic field was active between 4.6 and 3.8 Ma [Delaney and Gartner, 1997]. This volcanic field is part of a larger occurrence of Cenozoic basaltic volcanism in the Colorado Plateau and Basin and Range provinces but is distinct from many other fields as it has been eroded to a depth of \sim 800 m, based on its age and late Cenozoic erosion rates [Pederson et al., 2002, e.g.]. The sill-and-dike swarm, or volcanic plumbing system, cut a Jurassic sedimentary section from the Carmel Formation through the Cutler Formation. Diabasic dikes in this area trend 335° to 0° (relative to north) along regional joint sets, indicating low horizontal deviatoric stress during emplacement [Delaney and Gartner, 1997]. Sills in the San Rafael Swell range from <5 m to >40 m thick and are exposed in cliff sides and canyons in outcrops that extend for 100s-1000s m. This shallow magma plumbing system has been mapped [Delaney and Gartner, 1997], and used to improve our understanding of (i) dike emplacement [Delaney et al., 1986], (ii) magma diapirism in the shallow crust [Diez et al., 2009], and (iii) the spatial relationships between dikes and conduits [Kiyosugi et al., 2012], the latter of which are commonly surrounded by brecciated country rock, indicating conduit erosion during rapid magma ascent. Although Gartner [1986] described physical characteristics of exposed sills in the area, the complex emplacement processes of sills in this volcanic field have remained enigmatic. With the aid of lidar, we are able to document the complex map relationships between intrusions in the area.

4 Lidar Reconnaissance and Analysis

Terrestrial laser scanning (TLS), performed in 2010 and 2012, collected a 7.3 GB point cloud over an area of 5 km^2 . Both TLS surveys used Riegl terrestrial scanners. An airborne laser scanning (ALS) survey, in 2013, provided data for a 54 km^2 airborne laser swath map (ALSM) [Richardson, 2013], connecting the 2 TLS surveys into a single study area (Figure 1). Instrument specifications and data formats from these surveys are outlined in Table 3. Co-registering the coordinate systems of the three surveys creates a coverage area of $\sim 50 \text{ km}^2$, within which relief varies by up to 500 m. Thus, we are able to characterize the magma plumbing system in a tabular block approaching 25 km^3 in volume, which bounds the study area extent. This reconstruction of a magmatic plumbing system attempts to model the amount of magma emplaced into the crust due to Pliocene volcanism for the 25 km^3 space.

The three point clouds (two TLS and one ALSM) were consolidated and analyzed using LiDAR Viewer software [Kreylos et al., 2008]. Because the three-dimensional point cloud is so precise, lidar data help identify subtle changes in sill thickness over large areas, vertical

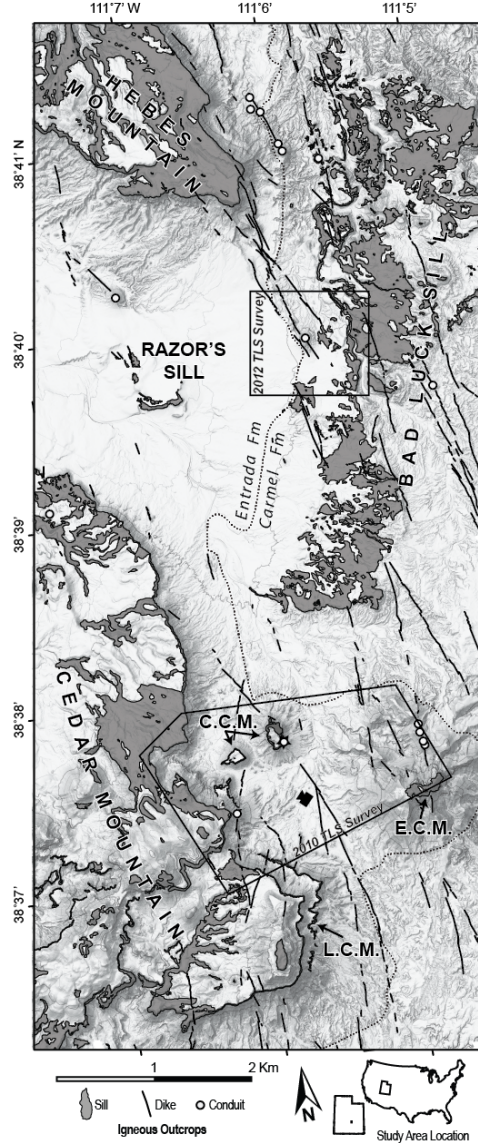


Figure 1: Shaded relief map of airborne laser scanning data, San Rafael Swell, Utah (USA) with formation contact and terrestrial laser scanning (TLS) areas labeled. Sills mapped are Hebes, Bad Luck, Razors, Cedar Mountain, Lower Cedar Mountain (LCM), Central Cedar Mountain (CCM), and East Cedar Mountain (ECM). Starred conduit symbol near CCM denotes conduit that was formed concurrently with CCM sill. Camera symbol near CCM is view location of Figure 2.

offsets in sills, and disrupted stratigraphy in overlying sedimentary units, which allow magma movements to be deduced. Contacts between igneous and sedimentary rocks are identified by shade contrast (igneous rocks are generally darker than sedimentary rocks in the near-infrared point cloud) and weathering patterns easily observable in the point cloud (Figure 5). Thickness measurements are made in LiDAR Viewer where sill upper and lower contacts are seen in close proximity. The exact locations of sill contacts are manually picked between points in the point cloud, where one point is interpreted as sill and the other as sedimentary rock (Table 4). Uncertainty at each measurement is determined as the average of point-to-point distances on top and bottom of the sill and is drastically reduced in areas where both TLS and ALSM data are available. Other measurements made in LiDAR Viewer include sill base elevations and strikes and dips of continuous sill segments and of sedimentary host rock below sills. Locations where sills abruptly change stratigraphic level are also mapped in the field. These abrupt changes can be traced between outcrops with point cloud measurements.

Sill exposures are mapped using 1 m National Agriculture Imagery Program (NAIP) images and the ALSM digital elevation model (DEM). These are combined with thickness measurements to estimate terminal boundaries of sills. The lateral edges of sills are not commonly preserved in outcrop, so we have estimated the terminal boundary of each sill to extend no more than 0.5 km from current exposures. Sills commonly crop out at cliffs with little horizontal exposure area (Figure 2), and by assuming that the mapped sills are contiguous between these outcrops, mapped sill areas are relatively small in comparison to interpreted sill areas (Table 1). Sill volume and average thickness are modeled by constraining the thicknesses of sills at their respective modeled boundaries to be 0 m and interpolating a Laplacian-spline surface within sill boundaries, calibrated to the measured thicknesses (Figures 3 and 6). Results from mapped and modeled areas, and maximum measured thicknesses, are detailed in Table 1.

Using aerial images and field mapping, Kiyosugi et al. [2012] mapped 16 conduits and 180 vertical, en echelon dike segments, with a cumulative length of 53 km, that crop out in the study area (Figure 1). The cumulative volume of igneous material stored in dikes is estimated to be the product of dike length, the modeled block height, and 85 cm, the modal dike thickness [Delaney and Gartner, 1997]. This might be a slight overestimate as some dikes might not have cut through the entire block height. The volume stored in conduits is the product of the surface area, mapped with the ALSM DEM and NAIP images, of each conduit and the modeled block height. This assumes conduit thickness does not change within the vertical limits of this reconstruction and might underestimate volume if conduits widen toward the surface or formed above the present-day surface.

5 Igneous System Reconstruction

Seven isolated sills crop out within the study area. We interpret these sills to have been emplaced independently as a result of single dike injections, based on evidence described below. Sill volumes range from 10^{-4} - 10^{-1} km³ and have been emplaced over areas of 10^{-1} to tens of square kilometers (Table 1). Through modeling sill geometries, we find that ~ 0.4 km³ of igneous material is permanently stored in the sills, representing 93% of all intrusive rocks in our reconstructed volume. Table 2 summarizes mapped areas and modeled volumes

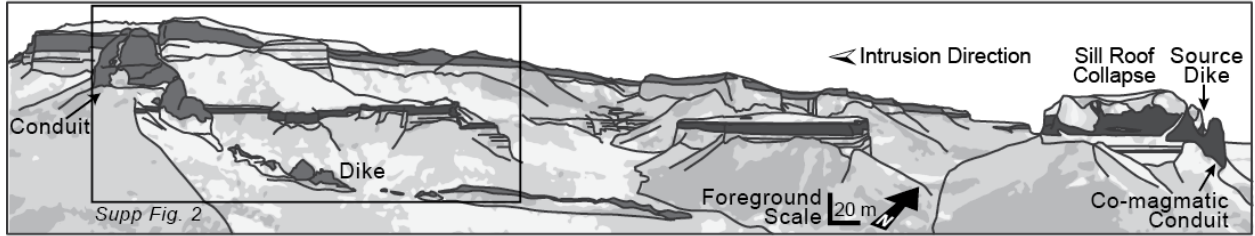


Figure 2: Northwest-facing panoramic diagram of Central Cedar sill, shaded dark gray (see Figure 1 for location). Other igneous intrusions are lighter gray, including sill capping Cedar Mountain (background), a conduit, and a dike.

Table 1: Areas, Thickness, and Volumes for 7 Sills in the Eroded San Rafael Swell Volcanic Field

Sills	Observations		Modeled values		
	Mapped area* (10^3 m 2)	Max thickness*	Modeled area (10^3 m 2)	Volume (km 3)	Mean thickness
Bad Luck	2901±141	19.0±0.2 m	13040	9.45×10^{-2}	7.3 m
Cedar Mountain	2782±149	40.7±0.2	25570	2.78×10^{-1}	10.9
Hebes	1919±45	36.1±0.1	5390	8.47×10^{-2}	15.7
East Cedar Mountain	39±2	N/A [†]	130	4.08×10^{-4}	3.0
Razor's	37±4	7.8±0.2	1270	1.62×10^{-3}	1.3
Central Cedar Mountain	26±5	15.5±0.1	880	4.42×10^{-3}	5.0
Lower Cedar Mountain	20±5	14.4±0.2	1030	5.44×10^{-3}	5.3

* Area uncertainty determined by assuming a 1-pixel-width error in mapping with 1-m basemap image. Thickness uncertainty calculation is discussed in the text.

† Sedimentary rocks are not observed above East Cedar Mountain Sill, inhibiting thickness measurements.

of sills, dikes, and conduits within the study area. By combining adjacent conduits along the same dike, we estimate that 12 distinct volcanic events are represented within the study area. Emplacement processes of sills and their role in the development of the Pliocene volcanic field can be further understood by investigating individual sills.

5.1 Hebes Sill

The sill at Hebes Mountain (Figure 1) is primarily preserved as a single 1.9 km^2 sill exposed over an area of $\sim 4 \text{ km}^2$. This sill generally dips with strata $1^\circ\text{-}8^\circ$ to the northwest, although locally some areas dip $5^\circ\text{-}30^\circ$ toward the center of the sill. Sill thicknesses are measured to a precision of $\pm 75 \text{ cm}$, with virtually all exposures measuring $>19 \text{ m}$. The sill thins monotonically from the center to the edges of Hebes Mountain, thinning most rapidly to the southwest.

By modeling Hebes sill as a 5.4 km^2 area, roughly following the shape of Hebes Mountain, the volume is estimated to be $8.5 \times 10^{-2} \text{ km}^3$. The elongate nature of this sill model (Figure 3), with increased thickness trending in the northwest dip direction is aligned in the regional dike direction, perhaps indicating a linear source region (dike) feeding the sill.

5.2 Central Cedar Sill

The Central Cedar sill caps two buttes to the east of Cedar Mountain and is exposed on the east facing cliffs of Cedar Mountain (Figure 2). The outcrops are interpreted to be parts of a single sill, as their basal contacts project across the small valleys between each exposure at the same elevation. Measured thicknesses of the Central Cedar Sill are 2-15 m, with basal contacts that dip with sedimentary host rock, at $2\text{-}5^\circ$ WNW to SW. The sill outcrops adjacent to a conduit associated with a $\sim 2 \text{ km}$ long dike on Central Cedar Mountain. Basalt between the conduit and sill appears continuous, with no brecciation, suggesting the dike and sill were formed cotemporally, and were thus comagmatic.

The average uncertainty in thickness measurements for Central Cedar Sill is $<20 \text{ cm}$, due to coverage from both ALSM and TLS data sets. The point cloud also enables the mapping of curvilinear “step-up” features, defined by Gartner [1986] as vertical offsets between different intrusion pathways, or feathers. Flow direction during intrusion is interpreted to be parallel to step-ups. Step-ups in this sill indicate flow to the W-WNW, away from and/or toward, the conduit. Modeling this sill as a tongue-shaped body intruding to the west from the suspected source dike (Fig S1, top center), Central Cedar Sill has an areal extent of $\sim 0.88 \text{ km}^2$, and a total volume of $4.4 \times 10^{-3} \text{ km}^3$ (Table 1).

A linearly thinning trend away from the conduit is evident in the sill, continuing for 1 km to the observed sill limit (Figure 4). Within 100 m of the conduit, sill thickness changes dramatically due to the presence of rotated sandstone blocks with thin basalt lenses injected over the tops of the sandstone blocks, indicating roof collapse into the sill (Figure 2). From these observations we conclude that the Central Cedar Sill was fed from a single dike and was emplaced in a tongue-like fashion to the west in its initial dipping direction. Further, we infer that a conduit-forming volcanic event may have halted further advance of the sill and subsequent flow of magma from the sill into the conduit caused the observed conduit-adjacent roof collapse.

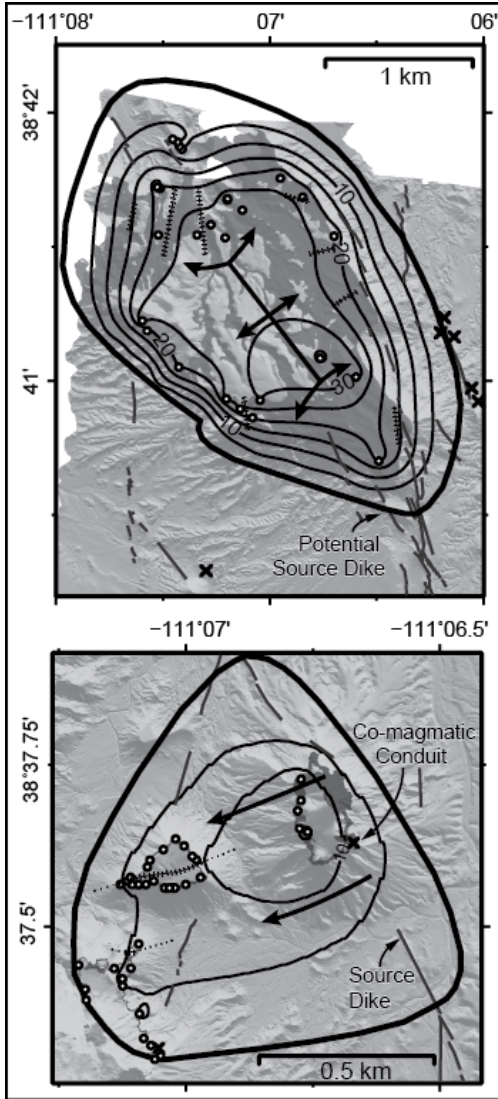


Figure 3: Sill thickness contour plots of Hebes (top) and Central Cedar (bottom) sills. White circles show measurement locations; X symbols are mapped conduits; gray lines are dikes; shaded areas are mapped sills. Thick lines with arrows indicate inferred direction of magma injection; hashed and dotted lines indicate mapped and inferred vertical sill offsets, respectively. Thick contours mark modeled sill boundaries where thickness is modeled to be 0 m.

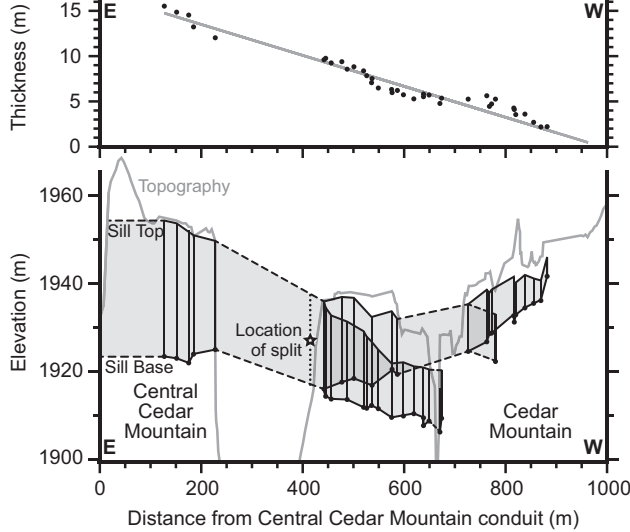


Figure 4: Top: Measured thicknesses of Central Cedar sill with respect to distance from conduit on Central Cedar Mountain with superimposed linear trend. All vertical errors are within size of plotted points. Bottom: Pseudocross section of Central Cedar sill superimposed on current topographic profile. Filled circles represent measured basal elevation (m above sea level) of sill; shaded area represents interpolated sill. Dotted line (star symbol) is inferred location where sill splits into two branches, manifested as step-ups in outcrop.

Table 2: Igneous Material Contributions in the Study Area

	Area (km^2)	Volume (km^3)	Vol% of intrusives
Sills	34.5	4.1×10^{-1}	92.9
Dikes	4.5×10^{-2}	2.2×10^{-2}	5.0
Conduits	1.9×10^{-2}	9.5×10^{-3}	2.1
Total	34.6	4.5×10^{-1}	1.8
Model Space	50.0	25.0	—

6 Discussion and Conclusions

Through lidar mapping of the San Rafael study area, seven sill-forming events in the shallow crust and 12 conduit-forming events have been identified and mapped in detail (Figure 1). We model the total volume of igneous material stored in sills to be 0.4 km^3 within a 25 km^3 block. This sill volume represents 93% of the stored igneous volume in the block, with the remaining 7% in dikes and conduits. There is no doubt that, volumetrically, sills are a critical component of the magma plumbing system in this distributed volcanic field.

It is possible, in fact, that sill volume in the San Rafael Swell volcanic field is comparable to erupted volume. Eruption volumes for the 12 conduits cannot be directly observed, as those lavas are completely eroded away. Eruption volumes for monogenetic volcanoes in similar fields span three orders of magnitude, ranging from 10^{-3} to 10^{-1} km^3 [Crowe et al., 1983, Condit et al., 1989, Kiyosugi et al., 2012, e.g.]. If we assume that average eruption volume is 0.1 km^3 for conduits in the San Rafael Swell, $\sim 1.2 \text{ km}^3$ of basalt would have been erupted at the surface, four times the estimated sill volume. Again, this comparison suggests that, volumetrically, crustal storage of magma in sills is a major feature of the magmatic system.

The general shape of the mapped sills in this field does include a thick center of several to tens of meters in height, tapering edges, and horizontal dimensions of one to several kilometers. While smaller sills exhibit a monotonic decrease in thickness from their interiors (Figure 4), the thickness profiles of larger sills are more complex and multiple thickened zones exist (Figure 6). The irregular shapes and size range of these sills might suggest that all sills in this area are the product of single injection events and are not polygenetic [Gudmundsson, 2012]. Furthermore, the maximum observed thicknesses of each of these sills are not highly correlated to the exposed or modeled areas of each sill. Sills in this area generally ascend stratigraphy only after lifting the roof, enabling exploitation of new bedding planes, suggesting that initial emplacement at this depth was a pressure-driven process, similar to the intrusion of the Trachyte Mesa laccolith (Henry Mountains, Utah, USA) [Wetmore et al., 2009]. Because horizontal deviatoric stress was low in this area during the Pliocene [Delaney et al., 1986], the minimum compressive stress direction could have significantly migrated from horizontal at 1 km depth, enabling sill formation given local stress conditions influenced by overlying topography [Gudmundsson, 2012].

The development of shallow sills likely affected eruption dynamics. If a comagmatic sill is present during a volcanic eruption, ascending bubbles can become concentrated in the vertical conduit at the conduit-sill junction by disproportional capture of the liquid phase of a two-phase flow in the horizontal branch [Conte, 2000]. This concentration occurs if overall magma flux is sufficiently low. The presence of the sill, therefore, enables modulation of explosive potential, with low magma flow rates resulting in more explosive activity than if a sill was not present. Following the method of Pioli et al. [2009], assuming a magma density of 2800 kg/m^3 , we calculate the transition flux to be $1.8 \times 10^5 \text{ kg/s}$ within the Central Cedar Mountain conduit (diameter 25 m), where lower flux would have concentrated bubbles in the conduit system. As average mass eruption rate for strombolian eruptions is commonly observed to be $10^3\text{-}10^5 \text{ kg/s}$ [Pioli et al., 2009], the presence of sills at the level where H_2O exolves critically impacts volcanic hazard.

Sills have been identified as a major instigator of unrest in association with stratovolcanoes [Biggs et al., 2010, Tarasewicz et al., 2012, e.g.], volcanic calderas [Macedonio et al.,

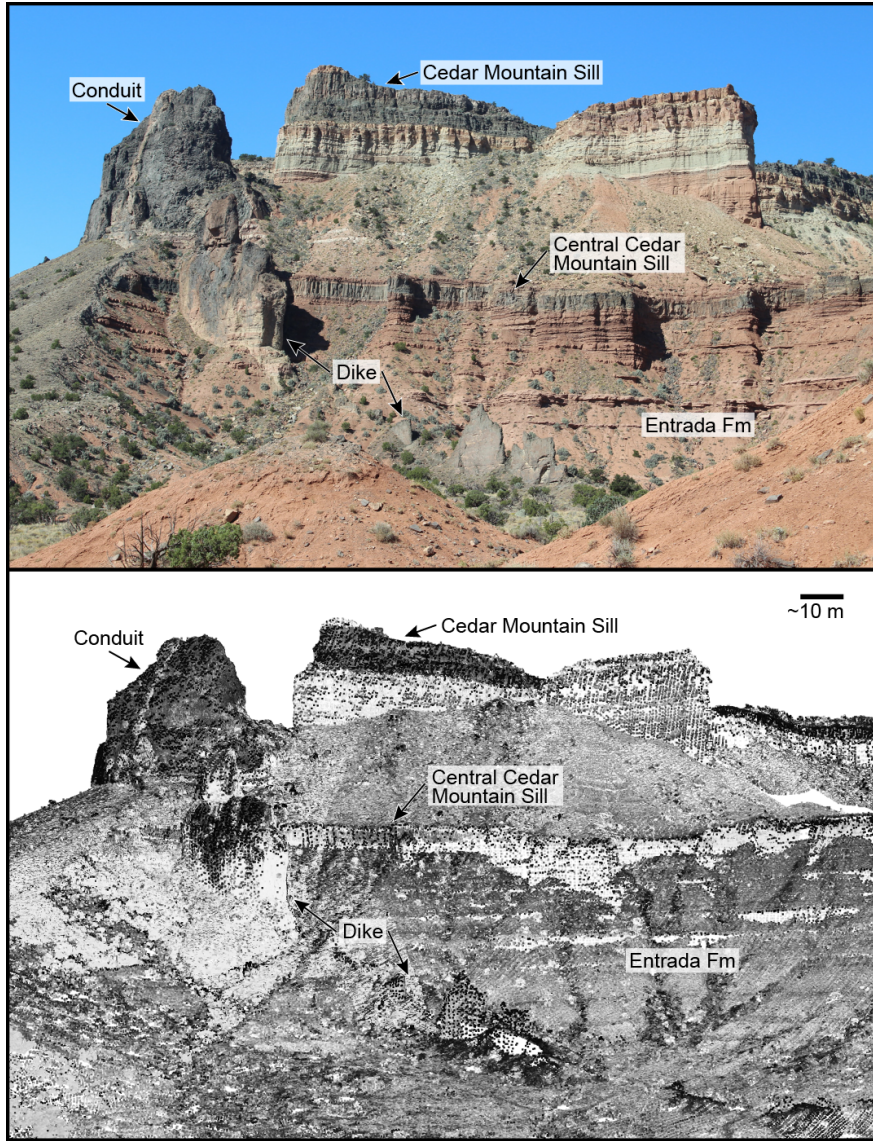


Figure 5: Top: Photograph of the east face of Cedar Mountain featuring Central Cedar Sill, Cedar Mountain Sill, and a dike which cross-cuts Central Cedar Sill. Sills are separated by dozens of meters by sedimentary rock. Photograph courtesy of J. McIlrath. Bottom: Combined TLS and ALS point cloud of the same view. Near-Infrared intensity differentiates between igneous and sedimentary rocks.

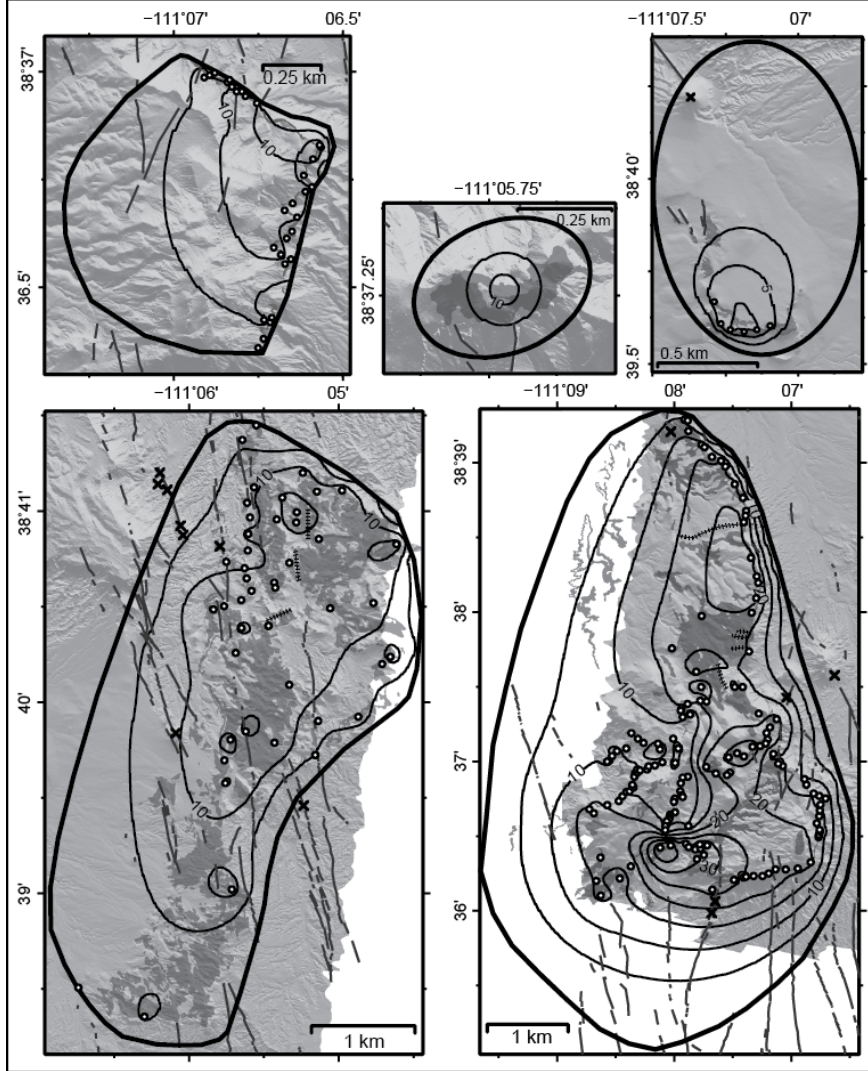


Figure 6: Contour plots of thickness models over ALSM hillshade data for additional sills. White circles are measurement locations; Xs are mapped conduits; gray lines are dikes; shaded areas are mapped sills. Thick lines with arrows indicate the inferred direction of magma injection and hashed/dotted lines indicate mapped/inferred vertical sill offsets. Top row, left to right sills are: Lower Cedar, East Cedar Mountain, Razors; Bottom row, left to right: Bad Luck, Cedar Mountain. Contour intervals are 5 m thickness except Razors sill where contours are every 2.5 m. Thick contours mark the modeled sill boundaries where sill thickness is modeled to be 0 m thickness. Note change in map scale.

2014], and monogenetic volcanic eruptions [Erlund et al., 2010]. The observation in the San Rafael Swell that the vast majority of igneous rock at 1 km depth is contained in sills suggests that similar deformation events may be precursory to volcanic eruptions in some active volcanic fields. Monitoring of active volcanic fields may benefit from use of deformation networks to detect sill emplacement in the shallow crust.

7 Acknowledgments

This project would not have been possible without the support of David Phillips and UNAVCO for lidar field equipment and data processing assistance. The TLS data acquisition project was funded by a grant from the National Science Foundation (EAR-0910696). ALS data acquisition and processing was completed by the National Center for Airborne Laser Mapping (NCALM) with funding provided by NSF's Division of Earth Sciences, Instrumentation and Facilities Program (EAR-1043051). M. Oskin and O. Kreylos of UC Davis are thanked for their help regarding LiDAR Viewer. USF students and faculty, Judy McIlrath, Kaz Mannen, Koji Kiyosugi, James Wilson, Samantha Kinman, and Travis Doering are thanked for field assistance. Helpful comments from K. Cashman, A. Gudmundsson, and an anonymous reviewer improved this manuscript.

References

- J. Biggs, P. Mothes, M. Ruiz, F. Amelung, T.H. Dixon, S. Baker, and S.-H. Hong. Stratovolcano growth by co-eruptive intrusion: The 2008 eruption of Tungurahua Ecuador. *Geophysical Research Letters*, 37(21), 2010. doi: 10.1029/2010GL044942.
- K.V. Cashman and S.M. McConnell. Multiple levels of magma storage during the 1980 summer eruptions of Mount St. Helens, WA. *Bulletin of Volcanology*, 68(1):57–75, 2005. doi: 10.1007/s00445-005-0422-x.
- C. D. Condit, L. S. Crumpler, J. C. Aubele, and W. E. Elston. Patterns of volcanism along the southern margin of the Colorado Plateau: The Springerville Field. *Journal of Geophysical Research*, 94(B6):7975–7986, 1989. doi: 10.1029/JB094iB06p07975.
- Charles B. Connor. Cinder Cone Clustering in the TransMexican Volcanic Belt: Implications for Structural and Petrologic Models. *Journal of Geophysical Research*, 95(B12):19,395–19,405, 1990. doi: 10.1029/JB095iB12p19395. doi:10.1029/JB095iB12p19395.
- G. Conte. *An experimental study for the characterisation of gas/liquid flow splitting at T-junctions*. PhD thesis, The University of Nottingham, 2000.
- B. Crowe, S. Self, D. Vaniman, R. Amos, and F. Perry. Aspects of potential magmatic disruption of a high-level radioactive waste repository in southern Nevada. *The Journal of Geology*, pages 259–276, 1983.
- P.T. Delaney and A.E. Gartner. Physical processes of shallow mafic dike emplacement near the San Rafael Swell, Utah. *Geological Society of America Bulletin*, 109(9):1177–1192, 1997. doi: 10.1130/0016-7606(1997)109<1177:PPOSMD>2.3.CO;2.
- P.T. Delaney, D.D. Pollard, J.I. Ziony, and E.H. McKee. Field relations between dikes and joints: emplacement processes and paleostress analysis. *Journal of Geophysical Research: Solid Earth*, 91(B5):4920–4938, 1986. doi: 10.1029/JB091iB05p04920.

- M. Diez, C.B. Connor, S.E. Kruse, L.J. Connor, and I.P. Savov. Evidence of small-volume igneous diapirism in the shallow crust of the Colorado Plateau, San Rafael Desert, Utah. *Lithosphere*, 1(6):328–336, 2009. doi: 10.1130/L61.1.
- E.J. Erlund, K.V. Cashman, P.J. Wallace, L. Pioli, M. Rosi, E. Johnson, and H.D. Granados. Compositional evolution of magma from Parícutin Volcano, Mexico: the tephra record. *Journal of Volcanology and Geothermal Research*, 197(1):167–187, 2010. doi: 10.1016/j.jvolgeores.2009.09.015.
- A.E. Gartner. *Geometry, Emplacement History, Petrography and Chemistry of a Basaltic Intrusive Complex, San Rafael and Capitol Reef Areas, Utah*. US Department of the Interior, Geological Survey, 1986.
- Agust Gudmundsson. Magma chambers: Formation, local stresses, excess pressures, and compartments. *Journal of Volcanology and Geothermal Research*, 237:19–41, 2012.
- K. Kiyosugi, C.B. Connor, P.H. Wetmore, B.P. Ferwerda, A.M. Germa, L.J. Connor, and A.R. Hintz. Relationship between dike and volcanic conduit distribution in a highly eroded monogenetic volcanic field: San Rafael, Utah, USA. *Geology*, 40(8):695–698, 2012. doi: 10.1130/G33074.1.
- O. Kreylos, G.W. Bawden, and L.H. Kellogg. Immersive Visualization and Analysis of LiDAR Data. In George Bebis, Richard Boyle, Bahram Parvin, Darko Koracin, Paolo Remagnino, Fatih Porikli, Jörg Peters, James Klosowski, Laura Arns, YuKa Chun, Theresa-Marie Rhyne, and Laura Monroe, editors, *Advances in Visual Computing*, volume 5358 of *Lecture Notes in Computer Science*, pages 846–855. Springer Berlin Heidelberg, 2008. doi: 10.1007/978-3-540-89639-5_81.
- G Macedonio, F Giudicepietro, L D'Auria, and M Martini. Sill intrusion as a source mechanism of unrest at volcanic calderas. *Journal of Geophysical Research: Solid Earth*, 119(5):3986–4000, 2014.
- J.L. Pederson, R.D. Mackley, and J.L. Eddleman. Colorado Plateau uplift and erosion evaluated using GIS. *GSA TODAY*, 12(8):4–10, 2002.
- L. Pioli, B.J. Azzopardi, and K.V. Cashman. Controls on the explosivity of scoria cone eruptions: Magma segregation at conduit junctions. *Journal of Volcanology and Geothermal Research*, 186(3-4):407 – 415, 2009. ISSN 0377-0273. doi: <http://dx.doi.org/10.1016/j.jvolgeores.2009.07.014>.
- J.A. Richardson. San Rafael, UT: Survey of exposed subsurface volcanic features, August 2013. doi: 10.5069/G908638S.
- R. Scandone, K.V. Cashman, and S.D. Malone. Magma supply, magma ascent and the style of volcanic eruptions. *Earth and Planetary Science Letters*, 253(3):513–529, 2007. doi: 10.1016/j.epsl.2006.11.016.

Jon Tarasewicz, Robert S White, Andrew W Woods, Bryndís Brandsdóttir, and Magnús T Gudmundsson. Magma mobilization by downward-propagating decompression of the eyjafjallajökull volcanic plumbing system. *Geophysical Research Letters*, 39(19), 2012.

P.H. Wetmore, C.B. Connor, S.E. Kruse, S. Callihan, G. Pignotta, C. Stremlan, and A. Burke. Geometry of the Trachyte Mesa intrusion, Henry Mountains, Utah: Implications for the emplacement of small melt volumes into the upper crust. *Geochemistry, Geophysics, Geosystems*, 10(8), 2009. doi: 10.1029/2009GC002469.

Table 3: Lidar Survey Specifications

Survey Date	Instrument	Camera	Instrument Accuracy/Misfit*	Points per m ²	Data Format
June 2010	Riegl LMS-Z620	Nikon D200	10 mm/13 cm standard misfit between tiepoints	49	XYZRGBI ASCII
May 2012	Riegl VZ-400	Nikon D200	5 mm/11 cm standard misfit between tiepoints	148	XYZRGBI ASCII
August 2013	Optech Gemini ALTM	N/A	5-35 cm/5cm interswath misfit	6.25	LAS

* Misfit in Riegl point clouds are reported after Georeferencing to WGS84 in RiSCAN Pro 1.8.0.

Table 4: Sill Thickness Measurements made in Lidar Viewer

Cedar Mountain Sill		
Easting*	Northing*	Thickness
489663 m	4274770 m	21.28±0.10 m
489243	4275170	16.39±0.74
489144	4275170	14.35±0.22
488668	4275360	11.95±0.15
488367	4275650	18.56±0.17
488735	4276050	19.51±0.12
488524	4278480	7.38±0.49
488565	4278470	1.85±0.28
488574	4278340	9.08±0.30
488736	4278170	12.58±0.21
488774	4278140	13.88±0.26
488867	4278020	13.42±0.15
488979	4277970	14.78±0.13
489031	4277900	15.47±0.20
489147	4277680	18.52±0.49
489249	4277510	16.47±0.28
489288	4277350	17.82±0.20
489282	4277290	18.27±0.14
489258	4277210	19.37±0.38
489348	4276770	24.83±0.42
489420	4276540	21.68±0.33
489438	4276460	20.01±0.52
489412	4276270	22.84±0.29
489356	4276090	18.12±0.15
489322	4275610	15.10±0.05
489442	4274840	16.60±0.15
489579	4274670	22.89±0.21
489538	4274600	22.18±0.18
489551	4274520	23.53±0.14
489528	4274470	23.81±0.17
489456	4274440	24.55±0.10
489363	4274430	27.37±0.15
489257	4274310	27.51±0.29
489173	4274350	27.05±0.15
489067	4274300	26.20±0.29
489083	4274110	22.68±0.16
489046	4274080	22.26±0.15
488908	4274100	18.50±0.32
488790	4274180	23.49±0.21
488729	4275170	24.68±0.07
488717	4275000	15.07±0.21
488560	4274960	15.52±0.16
488486	4274910	14.51±0.31
488475	4274880	13.79±0.33
488499	4274800	11.41±0.32
488795	4274990	20.09±0.12
488590	4274830	5.90±0.17
488379	4274530	5.10±0.15
488443	4274410	2.68±0.13
488537	4273230	32.87±0.15
488571	4273190	28.87±0.16
488653	4273160	33.31±0.20
488716	4273170	33.71±0.29
488710	4273220	33.13±0.28
488800	4273210	32.62±0.32
488759	4273090	33.61±0.34
488673	4273040	29.92±0.31
488863	4272660	27.55±0.10
489132	4272780	28.60±0.34
489249	4272810	22.32±0.23
489281	4272820	26.53±0.33
489375	4272830	21.53±0.46
489486	4272830	25.26±0.46
489563	4272860	20.21±0.48
489647	4272910	23.20±0.21
489772	4272910	20.86±0.30
489922	4272920	21.32±0.17
490081	4273000	21.64±0.10
490130	4273110	18.55±0.57
490180	4273310	17.58±0.21
490186	4273340	12.63±0.11
490198	4273380	23.08±0.43
490194	4273400	18.06±0.13
490158	4273480	17.68±0.28
490189	4273570	18.70±0.31
490197	4273640	15.89±0.52
490206	4273710	13.05±0.35

Central Cedar Mountain Sill					
	Easting	Northing	Thickness		
490268	4273790	13.68±0.46	487897	4274060	10.22±0.49
490191	4273820	14.27±0.32	487936	4274110	8.76±0.17
490121	4273850	14.66±0.10	487933	4274150	10.36±0.41
490030	4273960	13.01±0.30	487967	4274140	8.97±0.32
490007	4274030	9.51±0.45	488056	4274150	7.81±0.57
489738	4274190	15.53±0.12	488074	4274190	6.97±0.34
489683	4274220	17.17±0.11	488153	4274200	6.45±0.33
489622	4274340	12.12±0.14	488244	4274240	7.56±0.23
488560	4274060	5.60±0.24	488405	4274230	4.15±0.35
488499	4274050	6.00±0.21	488216	4274400	17.30±0.15
488474	4273980	5.63±0.14	488190	4274470	9.90±0.44
488468	4273880	5.34±0.11	488011	4274480	6.16±0.28
488485	4273830	4.63±0.15	487943	4274530	6.22±0.27
488497	4273810	5.91±0.09	487863	4274600	5.83±0.11
488399	4273790	6.38±0.26	487798	4274410	8.82±0.22
488388	4273750	6.87±0.41	487683	4274380	10.90±0.36
488401	4273620	6.85±0.29	487624	4274320	10.12±0.44
488340	4273590	7.07±0.21	487562	4274250	8.39±0.22
488335	4273560	8.97±0.26			
488328	4273530	7.77±0.22			
488297	4273510	9.19±0.18			
488282	4273450	8.85±0.10	489772 m	4274800 m	3.54±0.03 m
488279	4273400	9.19±0.22	489756	4274790	3.61±0.04
488567	4273450	9.62±0.37	489745	4274830	4.26±0.04
488218	4273180	40.57±0.15	489724	4274850	4.10±0.16
488347	4273210	40.70±0.21	489887	4275310	9.61±0.11
487479	4272590	16.55±0.26	489875	4275360	9.77±0.30
487422	4272770	15.22±0.05	489863	4275370	9.25±0.22
487851	4272950	17.97±0.24	489840	4275400	9.38±0.25
487715	4272800	12.68±0.14	489816	4275420	8.84±0.02
487476	4273060	17.94±0.28	489781	4275390	7.52±0.42
487395	4273610	19.54±0.19	490174	4275590	12.02±0.08
487339	4273660	15.05±0.52	490174	4275530	13.22±0.10
487561	4273710	13.93±0.61	490193	4275440	15.53±0.12
487705	4273760	12.85±0.67	489688	4275050	5.27±0.13
487749	4273820	12.20±0.36	489664	4275000	4.73±0.16
487796	4273870	12.40±0.36	489710	4275120	5.37±0.21
487838	4273880	8.61±0.23	489640	4275050	4.47±0.29
487885	4273930	9.51±0.46	489538	4275060	2.71±0.33
487872	4273960	9.87±0.44	489557	4274990	2.20±0.14

489560	4274960	2.23±0.38	489234	4281740	20.80±0.23
489808	4275280	7.85±0.20	489558	4281520	27.48±0.34
489784	4275280	6.49±0.16	489651	4281450	27.57±0.31
489753	4275300	6.32±0.13	489786	4281510	30.38±0.30
489731	4275290	5.75±0.09	489736	4281390	22.64±0.34
489710	4275290	5.28±0.26	488987	4282060	27.73±0.14
489691	4275290	5.52±0.22	489096	4282650	21.33±0.29
489678	4275300	5.72±0.15	489359	4282650	28.24±0.29
489658	4275290	4.78±0.23	489453	4282720	25.33±0.14
489743	4275360	5.98±0.43	489550	4282630	27.77±0.23
489735	4275340	6.21±0.17	489668	4282820	27.80±0.41
489687	4275310	5.82±0.66	489568	4282900	27.01±0.35
489845	4275290	8.57±0.20	489258	4283240	4.51±0.30
489814	4275280	8.38±0.14	489242	4283260	3.50±0.35
489798	4275280	7.08±0.17	489228	4283290	7.30±0.29
489712	4274920	5.26±0.18	489196	4283310	7.55±0.64
489663	4275020	5.62±0.17	489089	4282980	21.65±0.47
490165	4275500	14.55±0.31			
490170	4275450	14.87±0.10			

Razor's Sill		
Easting	Northing	Thickness
489464 m	4279070 m	5.7±0.11 m
489511	4279040	7.78±0.18
489580	4279030	7.25±0.08
489644	4279040	7.78±0.10
489710	4279060	5.81±0.11
489431	4279180	6.33±0.15

Hebes Sill		
Easting	Northing	Thickness
490593 m	4281090 m	22.58±0.16 m
490439	4281670	33.34±0.42
490194	4281800	36.08±0.10
490290	4282640	22.49±0.15
489926	4283040	24.07±0.32
490078	4282910	23.27±0.36
489565	4282890	26.61±0.18
489110	4282970	19.77±0.21
489020	4281990	20.72±0.20

Bad Luck Sill		
Easting	Northing	Thickness
492071 m	4280530 m	14.37±0.17 m
492785	4281840	15.32±0.12
491954	4282470	5.64±0.43
491820	4282330	4.81±0.20
491866	4281720	9.18±0.21
491892	4281580	7.93±0.25
492152	4281560	14.03±0.39
492342	4281530	16.49±0.38
492560	4281370	13.22±0.26
492275	4281140	12.17±0.29
493087	4280750	13.74±0.26
492940	4279650	8.36±0.32
492126	4280950	9.93±0.33
492137	4280900	11.57±0.36
491933	4281870	8.93±0.34
491641	4280720	11.42±0.27
491537	4280690	15.79±0.14
491753	4280270	13.25±0.30
492071	4280530	14.92±0.21
491643	4279230	13.02±0.14

491651	4279010	15.66±0.18	490319	4273650	12.62±0.14
491713	4277980	12.82±0.17	490353	4273680	12.53±0.44
490865	4276750	6.83±0.15	490408	4273730	10.52±0.13
490225	4277030	4.03±0.05	490436	4273750	9.95±0.35
493252	4280230	13.43±0.34	490401	4273800	8.95±0.23
493172	4280160	7.45±0.21	490441	4273870	12.06±0.20
492669	4280700	12.08±0.08	490475	4273920	11.19±0.20
492551	4279610	6.69±0.14	490469	4273930	13.32±0.18
492524	4279280	5.21±0.29	490200	4274110	12.37±0.45
492128	4279400	15.28±0.07	490151	4274140	13.21±0.16
491851	4279510	7.65±0.21	490136	4274160	7.59±0.25
491703	4279430	17.32±0.07	490113	4274160	14.43±0.45
493311	4281320	18.52±0.36	490093	4274180	10.50±0.45
492541	4281830	12.38±0.11	490073	4274200	5.39±0.19
492404	4282010	12.20±0.24	490083	4274210	3.20±0.15
492346	4281630	18.96±0.17	489974	4274220	10.40±0.36
492205	4281770	15.35±0.14	489997	4274230	4.38±0.26
491840	4281090	9.69±0.16	490019	4274240	2.85±0.16
491876	4281420	11.09±0.17	490204	4273060	1.88±0.24
491871	4281260	8.46±0.28			
491663	4281150	9.22±0.20			
491860	4280990	11.12±0.27			
491907	4280870	11.53±0.19			
491808	4280780	12.79±0.28			
491811	4280510	15.74±0.20			
492272	4279960	13.22±0.12			

* Eastings and northings reported in UTM Zone 12 coordinates.

Lower Cedar Mountain Sill		
Easting	Northing	Thickness
490227 m	4273100 m	1.26±0.13 m
490230	4273180	6.82±0.19
490256	4273170	2.26±0.23
490263	4273190	0.76±0.08
490320	4273420	9.44±0.26
490345	4273440	9.19±0.22
490302	4273460	10.71±0.35
490272	4273490	12.09±0.41
490327	4273530	8.57±0.20
490350	4273560	6.32±0.43
490372	4273620	10.26±0.16